Journal of Power Sources 186 (2009) 67–79

Contents lists available at ScienceDirect

Journal of Power Sources

journal homepage: www.elsevier.com/locate/jpowsour

The calibration of a model for simulating the thermal and electrical performance of a 2.8 kW_{AC} solid-oxide fuel cell micro-cogeneration device

Ian Beausoleil-Morrison*, Kathleen Lombardi

CANMET Energy Technology Centre, Natural Resources Canada, Ottawa, Canada

ARTICLE INFO

Article history:
Received 18 June 2008
Received in revised form 7 August 2008
Accepted 20 August 2008
Available online 11 September 2008

Keywords:
Solid-oxide fuel cell
Micro-cogeneration
Combined heat and power
Building simulation
Residential buildings
Model calibration

ABSTRACT

The concurrent production of heat and electricity within residential buildings using solid-oxide fuel cell (SOFC) micro-cogeneration devices has the potential to reduce primary energy consumption, greenhouse gas emissions, and air pollutants. A realistic assessment of this emerging technology requires the accurate simulation of the thermal and electrical production of SOFC micro-cogeneration devices concurrent with the simulation of the building, its occupants, and coupled plant components. The calibration of such a model using empirical data gathered from experiments conducted with a 2.8 kW_{AC} SOFC micro-cogeneration device is demonstrated. The experimental configuration, types of instrumentation employed, and the operating scenarios examined are treated. The propagation of measurement uncertainty into the derived quantities that are necessary for model calibration are demonstrated by focusing upon the SOFC micro-cogeneration system's gas-to-water heat exchanger. The calibration coefficients necessary to accurately simulate the thermal and electrical performance of this prototype device are presented and the types of analyses enabled to study the potential of the technology are demonstrated.

1. Introduction

Micro-cogeneration (also known as residential cogeneration and small-scale combined heat and power) is the concurrent production of electricity and heat from a single fuel source with electrical outputs of less than 10–15 kW. The concurrent production of electrical and thermal energy has the potential to reduce primary energy consumption, greenhouse gas emissions, and air pollutants associated with providing energy services to buildings. By generating electrical power within residential buildings, this emerging technology also has the potential to reduce electrical transmission and distribution inefficiencies and to alleviate utility peak demand problems. A number of manufacturers worldwide are developing micro-cogeneration devices based upon fuel cells, internal combustion engines, and Stirling cycles [1,2], while adoption of these technologies is being encouraged in many countries through financial incentives and favourable electricity tariff structures.

Micro-cogeneration devices have only modest fuel-to-electrical conversion efficiencies: some existing prototypes have efficiencies as low as 5% [3–5] (net AC electrical output relative to the source fuel's lower heating value (LHV)). Although solid-oxide fuel cell (SOFC) technologies have potential to deliver electrical efficiencies as high as 45% [6], these levels have not yet been realized in actual prototype devices. These electrical efficiencies are relatively low compared to combined-cycle central power plants (the state-of-the-art for fossil-fuel-fired central power generation), which can achieve efficiencies in the order of 55% [7,8]. Consequently, it is imperative that the thermal portion of the micro-cogeneration device's output be well utilized to supply the building's space heating, space cooling (through a thermally activated cycle), and/or domestic hot water (DHW) heating needs. If this thermal output cannot be exploited, micro-cogeneration will not compare favourably to the best-available central power generation technologies.

However, accurately analyzing the utilization of a micro-cogeneration device's thermal output is complicated by strong coupling between the micro-cogeneration unit, other thermal plant components, and the building's thermal and electrical demands. This complexity can be illustrated with a simple example that considers a micro-cogeneration unit that is configured to follow a house's electrical loads. Lighting and appliance demands may peak late in the evening, resulting in substantial thermal output from the micro-cogeneration unit. However, there may be little demand for space heating at this time as the house is allowed to cool slightly during the night. Similarly there may be little demand for DHW. Consequently, the system will likely integrate some storage device to hold the thermal energy until a demand exists. The volume and thermal characteristics of the storage tank, the occupant electrical and hot water usage patterns, the house's thermal charac-

* Corresponding author. Present address: Department of Mechanical and Aerospace Engineering, Carleton University, Ottawa, Canada.
E-mail address: Ian_Beausoleil-Morrison@carleton.ca (I. Beausoleil-Morrison).

0378-7753/$ – see front matter © 2008 Elsevier B.V. All rights reserved.
doi:10.1016/j.jpowsour.2008.08.098

teristics, and prevailing weather all influence whether this thermal energy output of the micro-cogeneration device will be exploited or wasted. The potential design and operational combinations of these factors are almost limitless. In order to accurately assess the performance of these emerging technologies, therefore, it is imperative that models of micro-cogeneration devices be incorporated into whole-building simulation tools that account for the types of interactions outlined above.

These factors motivated the formation of Annex 42 of the International Energy Agency's Energy Conservation in Buildings and Community Systems Programme (IEA/ECBCS) [5]. The objectives of this international collaborative effort were to develop simulation models that advance the design, operation, and analysis of micro-cogeneration systems, and to apply these models to assess the technical, environmental, and economic performance of the technologies. These objectives were accomplished by developing and incorporating models of micro-cogeneration devices within existing whole-building simulation programs such as ESP-r [9], EnergyPlus [10], and TRNSYS [11]. These models are more detailed than the simple performance-map methods that have been previously applied to assess micro-cogeneration and which cannot accurately treat the thermal coupling to the building and its thermal plant as outlined above (e.g. [12–24]).

One of the mathematical models developed by IEA/ECBCS Annex 42 is suitable for simulating the performance of SOFC micro-cogeneration devices [25,26]. This is a system-level model that considers the thermodynamic performance of all components that consume energy and produce the SOFC micro-cogeneration device's thermal and electrical output. The model requires calibration using empirical data that can be acquired from the testing of coherent systems or components and is designed for operation at a time resolution that is in the order of minutes.

This paper demonstrates how the IEA/ECBCS Annex 42 SOFC micro-cogeneration model can be calibrated using empirical data. This demonstration is performed using data gathered through experiments conducted on a prototype 2.8 kW_{AC} SOFC micro-cogeneration system. Pertinent aspects of the model are first reviewed. The experimental equipment and measurement methods employed to gather the calibration data are then presented. The propagation of measurement uncertainty into derived quantities is treated and the methods utilized to calibrate model inputs based upon these data are then elaborated. The calibration parameters which can be used in conjunction with the model to simulate the performance of this specific prototype are presented and then simulations are performed to demonstrate the use of the calibrated model. Concluding remarks are then provided.

2. Model description

This section describes only those aspects of the SOFC micro-cogeneration model that are the subject of the calibration procedures presented in Section 5. The interested reader is referred to [25] and [26] for a comprehensive exposition of the model.

2.1. Model topology

Fig. 1 illustrates one possible system configuration of a SOFC micro-cogeneration device. It is important to note that the fuel cell stack is only a single component within a complex energy conversion system. Besides the fuel cell stack (shown in grey), the system might include: an afterburner to combust unreacted fuel, an air filter and pre-heater, and a fuel desulfurizer, pre-heater, pre-reformer, and reformer. A compressor may be required to supply pressurized fuel while a blower will likely be present to supply air to provide oxygen to support the electrochemical and combustion reactions. The system will include a power conditioning unit to convert the SOFC's DC electrical output to AC. All SOFC micro-cogeneration systems will include a heat recovery device that transfers the heat of the hot product gases to the building's thermal plant to provide space heating, space cooling, and/or DHW heating.

As previously mentioned, numerous researchers have employed performance-map methods to study the integration of SOFC micro-cogeneration systems within buildings (e.g. [12–15,20,22]). These methods employ a performance map (derived either from empirical evidence or from detailed modelling performed outside the context of whole-building simulation) that decouples the electrical and thermal performance of the micro-cogeneration device from the rest of the thermodynamic system. In contrast to this, the model that is the subject of the current paper explicitly treats the interactions between the micro-cogeneration device and the building and its occupants on a time-step basis (typically in the order of minutes). It is worth noting that this model is much more simplistic than many detailed SOFC models presented in the literature (e.g. [27,28]), most of which are not well suited for the purposes of evaluating the energy performance of SOFC micro-cogeneration devices since they focus on single cells or stacks of cells while other components (refer to Fig. 1) are left untreated.

The model discretizes the SOFC micro-cogeneration system into groupings of components that comprise major sub-systems, such as those that produce electrical power, supply air, capture heat from hot product gases, etc. In this manner, once the model is calibrated for a specific SOFC micro-cogeneration device analyses can be conducted to explore the benefits of improving the performance of individual sub-systems. For example, the impact of improving the heat recovery device upon overall system performance can be simulated without recalibrating the portions of the model that represent the fuel cell power module (FCPM), power conditioner, and other sub-systems. Additionally, such a structure facilitates the future development of more detailed modelling methods for specific sub-systems.

The model discretizes the SOFC micro-cogeneration system into nine control volumes. Each control volume is modelled in as rigorous a fashion as possible given the constraints of computational efficiency and the need to calibrate model inputs based upon the testing of coherent systems. It is worth noting that the equations described in this section will be recalculated hundreds of thousands of times to perform a single annual simulation at 2 min time-steps.

The following sub-sections illustrate the modelling methods employed by focusing on two control volumes. One represents the exhaust-gas-to-water heat exchanger that produces the useful thermal output. The other control volume represents the fuel cell power module which includes the stack, after-burner, and the other components enclosed by the dashed line in Fig. 1.

2.2. Exhaust-gas-to-water heat exchanger

A schematic representation of the control volume encapsulating the device that transfers heat from the hot gases exiting the FCPM control volume to the water loop connected to the building's plant is shown in Fig. 2. The state point labels shown in the figure are used in the development that follows.

The sensible component of the heat transfer from the hot gases to the water is characterized with the log mean temperature difference (LMTD) method for counterflow heat exchangers,

$$q_{\text{sensible}} = (UA)_{\text{eff}} \frac{(T_{\text{g-in}} - T_{\text{w-out}}) - (T_{\text{g-out}} - T_{\text{w-in}})}{\ln\left(\frac{T_{\text{g-in}} - T_{\text{w-out}}}{T_{\text{g-out}} - T_{\text{w-in}}}\right)} \quad (1)$$

where $T_{\text{g-in}}$ is the temperature of the hot gases exiting the FCPM and entering the heat exchanger and $T_{\text{g-out}}$ is the temperature of

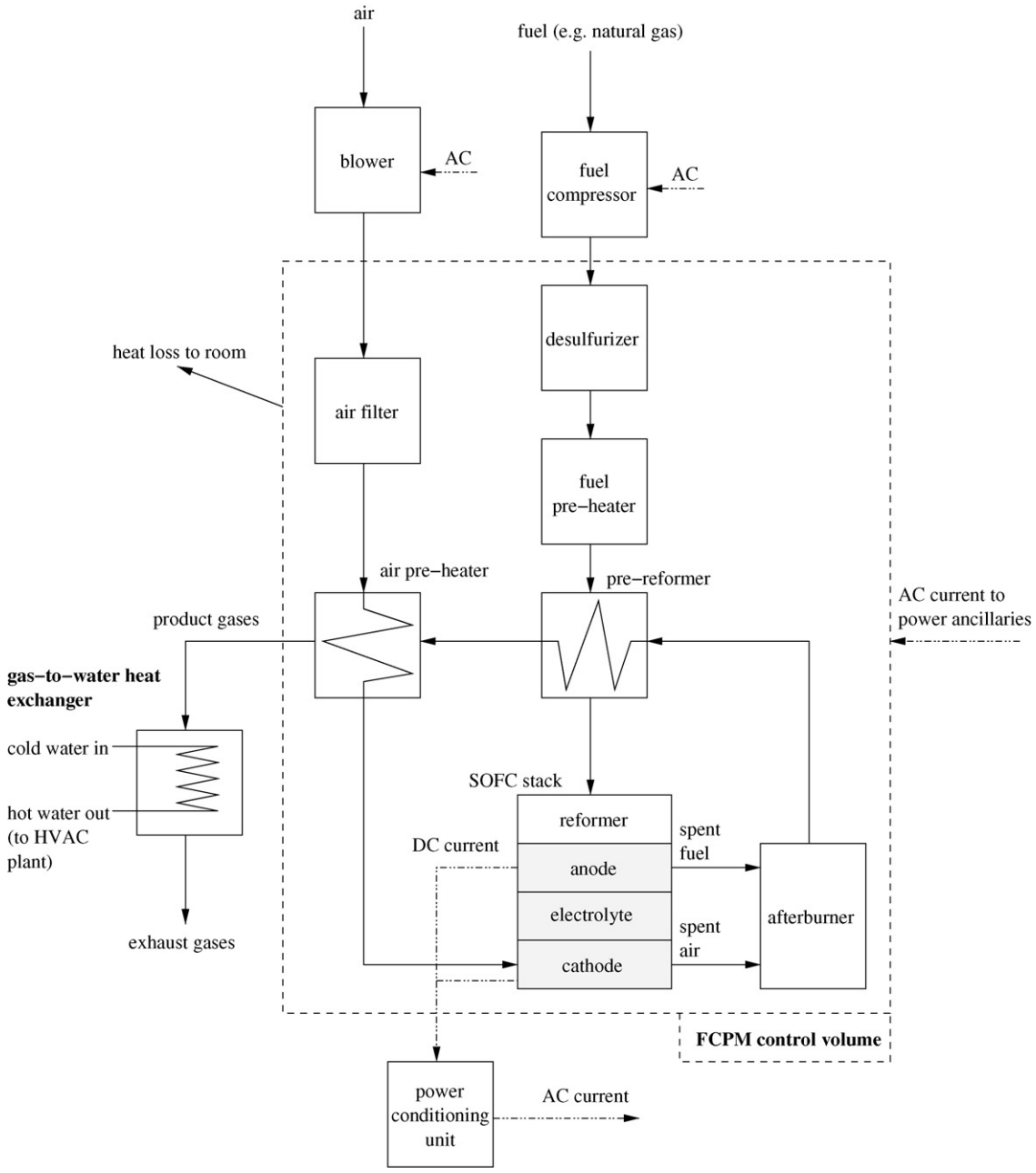

Fig. 1. One possible system configuration of a SOFC micro-cogeneration device.

the cooled gases exiting the heat exchanger. T_{w-in} is the temperature of the cold water at the heat exchanger inlet and T_{w-out} is the temperature of the warmed water exiting the heat exchanger. $(UA)_{eff}$ is the effective product of the heat transfer coefficient and area ($W\,K^{-1}$).

If it is assumed that heat loss from the heat exchanger to the ambient is negligible and that the heat capacity of each fluid stream remains constant through the heat exchanger, then the following energy balance can be written for the heat transfer between the fluid streams,

$$q_{sensible} = (\dot{N}\hat{c}_P)_{g-in}(T_{g-in} - T_{g-out}) = (\dot{N}\hat{c}_P)_{w-in}(T_{w-out} - T_{w-in}) \quad (2)$$

where $\hat{c}_P$ is the fluid's molar heat capacity ($J\,kmol^{-1}\,K^{-1}$) and $\dot{N}$ is its molar flow rate ($kmol\,s^{-1}$).

The $(UA)_{eff}$ value required by Eq. (1) must be evaluated at each time-step of the simulation. An approach is employed which casts it as a parametric relation of the water and product gas flow rates[1],

$$(UA)_{eff} = hx_{s,0} + hx_{s,1}\dot{N}_w + hx_{s,2}\dot{N}_w^2 + hx_{s,3}\dot{N}_g + hx_{s,4}\dot{N}_g^2 \quad (3)$$

where $hx_{s,i}$ are empirical coefficients characterizing a specific heat exchanger. The form of Eq. (3) facilitates the determination of the $hx_{s,i}$ coefficients from experimental data, as will be shown in Section 5.

The latent component of the heat transfer from the hot gases to the water is given by,

$$q_{latent} = \dot{N}_{H_2O-cond}\hat{h}_{H_2O,fg} \quad (4)$$

[1] Alternate approaches are available, as treated in [25] and [26].

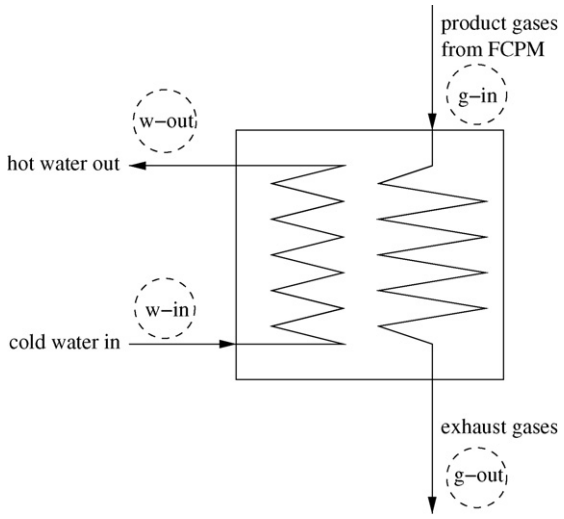

Fig. 2. Exhaust-gas-to-water heat exchanger control volume.

where $\dot{N}_{H_2O-cond}$ is the rate of condensation of water from the gas stream (kmol s^{-1}) and $\hat{h}_{H_2O,fg}$ is the molar heat of vapourization of water (J kmol^{-1}).

The rate of condensation is expressed in a parametric form that facilitates the determination of its coefficients from empirical data. The functional form of this parametric equation was established by recognizing that, for a given heat exchanger design, the rate of condensation will be primarily influenced by the concentration of water vapour in the gas stream and by the difference between the heat exchanger's temperature and the gas' dew point,

$$\dot{N}_{H_2O-cond} = (T_{cond-threshold} - T_{w-in}) \times \left[hx_{l,1} \left(\frac{\dot{N}_{H_2O}}{\dot{N}_{g-in}} \right) + hx_{l,2} \left(\frac{\dot{N}_{H_2O}}{\dot{N}_{g-in}} \right)^2 \right] \quad (5)$$

where $hx_{l,i}$ are empirical coefficients characterizing a specific heat exchanger. $\dot{N}_{H_2O}$ in Eq. (5) is the molar flow rate of water vapour in the gas stream entering the heat exchanger and $\dot{N}_{g-in}$ is the molar flow rate of all constituents of the gas.

$T_{cond-threshold}$ is a user-specified fixed value that represents the threshold of the water-inlet temperature above which condensation will not occur. When T_{w-in} is below $T_{cond-threshold}$ the condensation rate will be determined with Eq. (5). And when T_{w-in} is above $T_{cond-threshold}$ it is assumed that no condensation occurs.

The total heat recovery from the hot gases to the water (q_{HX}) is determined by summing the results of Eqs. (1) and (4).

$$q_{HX} = q_{sensible} + q_{latent} \quad (6)$$

Section 5 details the methods used to determine the $hx_{s,i}$ coefficients for Eq. (3) and the $hx_{l,i}$ coefficients and $T_{cond-threshold}$ for Eq. (5).

2.3. Fuel cell power module

The energy balance for the FCPM (indicated by the dashed line in Fig. 1) can be written in the following form[2],

$$\dot{H}_{fuel} + \dot{H}_{air} = P_{el} + \dot{H}_{g-in} + q_{skin-loss} + q_{FCPM\text{-}to\text{-}dilution} \quad (7)$$

where $\dot{H}_{fuel}$ and $\dot{H}_{air}$ represent the enthalpy carried into the control volume by fuel and air (for electrochemical and combustion reactions as well as excess air). P_{el} is the net DC power production, that is the stack power less ohmic losses in cabling and the power draw of ancillaries (e.g. the fan that supplies the air). $\dot{H}_{g-in}$ represents the enthalpy carried out of the control volume by the exiting gas stream, that is the hot products of the electrochemical and combustion reactions as well as the excess air and the inert constituents of the fuel. (This is also the inlet condition for the heat exchanger, as indicated in Eq. (1).) The final two terms in Eq. (7) represent thermal losses: $q_{skin-loss}$ is the radiant and convective heat transfer to the containing room while $q_{FCPM\text{-}to\text{-}dilution}$ represents the heat transfer from the FCPM to the air stream which is drawn through the micro-cogeneration device's cabinet to comply with gas venting requirements of safety codes.

As is common in the literature (e.g. [28,12]) the FCPM's electrical efficiency (ε_{el}) is expressed as the DC power production relative to the fuel's LHV,

$$\varepsilon_{el} = \frac{P_{el}}{\dot{N}_{fuel} LHV_{fuel}} \quad (8)$$

where $\dot{N}_{fuel}$ is the rate of fuel supply to the FCPM (kmol s^{-1}).

Since the model groups the fuel cell stack with other components such as the afterburner and heat exchangers into the FCPM control volume, it makes no attempt to simulate the electrochemical processes occurring within the fuel cell, but rather represents the performance of the FCPM using a parametric relation between the electrical efficiency and the net electrical power output[3],

$$\varepsilon_{el} = [\varepsilon_0 + \varepsilon_1 P_{el} + \varepsilon_2 P_{el}^2] \quad (9)$$

The term in Eq. (7) for the enthalpy of the inlet air stream represents a summation of the enthalpies of the constituent gases,

$$\dot{H}_{air} = \sum_i (\dot{N}_i \hat{h}_i)_{air} \quad (10)$$

where $\hat{h}_i$ is the molar enthalpy (J kmol^{-1}) and $\dot{N}_i$ is the molar flow rate (kmol s^{-1}) of gas constituent i (e.g. N_2, O_2).

As the form of Eq. (9) includes an implicit relationship between the fuel and air supply rates, the model employs an explicit relationship to determine the FCPM's excess air ratio. The excess air ratio (λ) is given by,

$$\lambda = \frac{\dot{N}_{air}}{\dot{N}_{air}^s} - 1 \quad (11)$$

where $\dot{N}_{air}$ is the air supply rate of the FCPM and equals $\sum_i \dot{N}_i$ (kmol s^{-1}). $\dot{N}_{air}^s$ is the air supply rate required to support stoichiometric electrochemical and combustion reactions of the fuel constituents.

A parametric function is used to relate the excess air ratio to the net electrical output[4],

$$\lambda = \frac{(a_0 + a_1 P_{el} + a_2 P_{el}^2)(1 + a_3 T_{air})}{\dot{N}_{air}^s} - 1 \quad (12)$$

where T_{air} is the temperature of the air (°C) supplied to the FCPM.

The form of Eq. (12) facilitates the determination of the a_i coefficients from experimental data, as will be shown in Section 5.

Eqs. (10–12) along with a polynomial equation that relates the enthalpy of gas constituents to temperature are used to establish the $\dot{H}_{air}$ term of Eq. (7) each time-step of the simulation. The

[2] Only terms that are relevant to the particular SOFC device treated in this paper are shown here for the sake of clarity.

[3] The model includes terms to represent the operational degradation as well as the impact of stop-start cycling, but these are not shown here for the sake of clarity.

[4] Alternate approaches are available, as treated in [25] and [26].

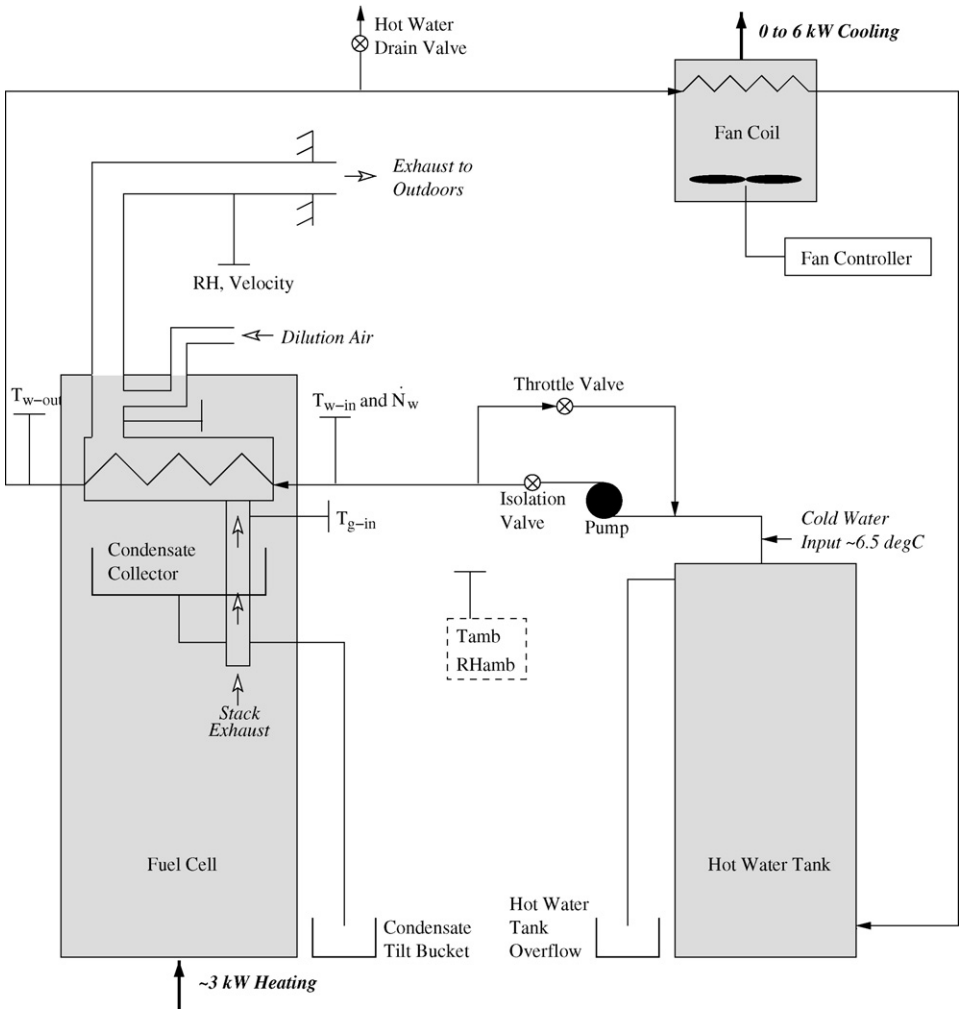

Fig. 3. Experimental configuration to control flow rate and temperature of water entering the heat exchanger.

remaining terms of this energy balance are resolved with similar techniques, which is then re-arranged and solved each time-step of the simulation to predict the temperature of the hot gases entering the exhaust-gas-to-water heat exchanger (refer to T_{g-in} in Eq. (7)).

The next section describes the experiments that were conducted with a prototype 2.8 kW_{AC} SOFC micro-cogeneration device in order to gather the data required to calibrate the model's empirical coefficients such as those of Eqs. (3), (5), (9), and (12).

3. Experimental and measurement procedures

An experimental programme was designed to examine the performance of the prototype 2.8 kW_{AC} SOFC micro-cogeneration device under a series of controlled boundary conditions according to a protocol established by IEA/ECBCS Annex 42 [29]. Many of these tests required control over the water flow rate through the SOFC micro-cogeneration device's heat exchanger and the water inlet temperature. The experimental set-up used to achieve this control is shown schematically in Fig. 3.

Water was pumped from a storage tank to the micro-cogeneration device's heat exchanger. From there the water flowed through a fan-coil before returning to the storage tank. As the circulating pump was operated at constant speed, the flow rate of water through the micro-cogeneration device's heat exchanger was controlled by manually setting a throttling vale. An isolation valve downstream of the pump was manually controlled to increase back pressure, enabling a further reduction in the water flow rate through the heat exchanger. The lowest steady water flow rate through the heat exchanger that could be be achieved was 4 L min^{-1}. The highest flow rate was limited by the pump's capacity and was approximately equal to 12 L min^{-1}.

The fan-coil was used to dissipate heat from the loop when the desired water temperature was greater than that of the room air. An on–off controller with a 0.2 °C dead-band cycled the fan-coil on when necessary to achieve the desired water inlet temperature at the micro-cogeneration device's heat exchanger. This resulted in a small degree of oscillation although the control was mostly satisfactory. When the desired water temperature was below that of the room air, warm water was drained downstream of the micro-cogeneration device. This volume of water was replenished by adding cold water from the mains to the tank. The minimum heat exchanger water inlet temperature was thus regulated by the temperature of the water mains (approximately 6 °C). The maximum temperature was restricted to 60 °C in order to protect the circulating pump.

Once steady conditions were achieved, measurements were logged to file for a period of time to provide sufficient data to analyze the statistical variation of the measured and derived quantities for each test. Fig. 4 illustrates the flow rate and heat exchanger water

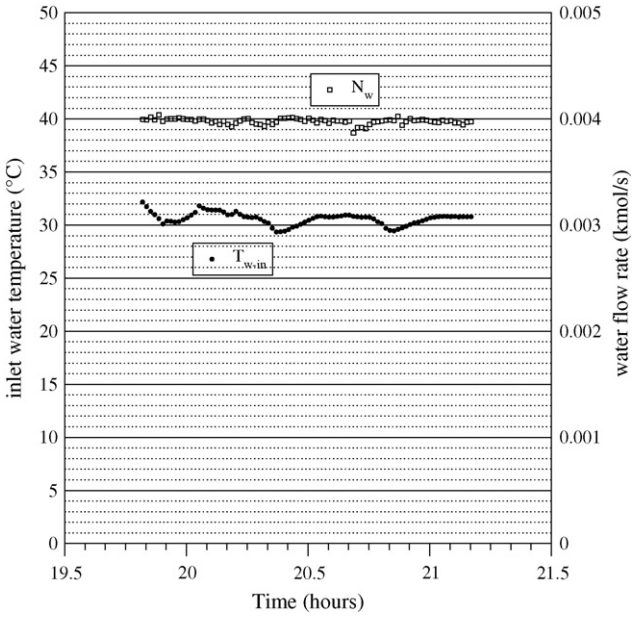

Fig. 4. T_{w-in} and $\dot{N}_w$ over duration of one test.

inlet temperature for the test that was configured to supply 30 °C water to the heat exchanger at the lowest flow rate possible. As can be seen from the graph, ideal steady conditions could not be maintained over the duration of the test. Control over the water flow rate was found to be more stable than that over the water inlet temperature. In general, steady thermal conditions were more difficult to achieve at lower entering water temperatures. Notwithstanding, the variations in the water inlet temperature were deemed to be acceptable. The impact of these variations upon derived quantities will be examined in Section 4.

In addition to experiments that controlled thermal boundary conditions, tests were performed in which the SOFC micro-cogeneration device's electrical output was modulated. This was achieved by varying the stack current demanded by the device's internal controller.

The micro-cogeneration device and the water loop were instrumented to record both electrical and thermal conditions throughout the tests. Voltage and current were measured at the points where power flowed to the power conditioning system, to the battery, and to the DC-powered ancillary devices (refer to Fig. 1). The AC output from the power conditioning system was also instrumented as were the AC-powered ancillary devices. Voltage taps were placed to measure DC voltage at the stack exit (i.e. at the start of the transmission cable carrying power to the PCU) and at the AC ancillary devices. A current shunt was installed to measure the total ancillary current draw. A watt transducer was used to monitor the AC output to the grid.

The flow rates of natural gas supplied to the FCPM's stack and burner (fired to maintain stack temperatures when necessary) were measured independently using two mass flow controllers. Two venturi pressure transducers were used to measure the flow rates of air to the stack and burner.

The flow rate of water through the heat exchanger was measured at its inlet using a turbine water flow meter. Type-T thermocouples were used to measure the temperature of the water at the heat exchanger inlet and outlet. Gas temperatures were measured at the heat exchanger inlet and outlet using type-K thermocouples.

Due to the heat exchanger's design, when water vapour condensed from the exhaust gases the water droplets would drip onto the thermocouple measuring T_{g-in} (refer to Fig. 2). This resulted in erroneous temperature readings, a fact that did not hinder model calibration efforts but rather assisted in identifying $T_{cond-threshold}$ in Eq. (5), as will be treated in Section 5. The micro-cogeneration device collects the condensate in an internal reservoir. When full, a float valve triggers a pump to drain this reservoir. A rain gauge tilt bucket was located to collect the pumped condensate to measure its volumetric flow rate. This gauge was calibrated to tilt for each accumulation of 8.24 mL of condensate.

The micro-cogeneration device is designed such that the cooled gases exiting the heat exchanger are mixed with the dilution air that is drawn through the cabinet to control skin losses to the containing room. The temperature, velocity, and relative humidity of these mixed gases were measured downstream of the mixing point. A velocity probe was used to measure the velocity of this gas stream. Due to the configuration of the micro-cogeneration device's exhaust chimney it was not possible to take these measurements in a region of fully developed flow. Rather, measurements had to be taken close to a 90° bend in the duct. During the exploratory phase of the work, the probe was inserted at numerous locations across the duct and the measured velocity profile examined to choose the most representative location to mount the probe. These limitations resulted in significant uncertainty in the measured flow rate of the combined gas stream.

Finally, the ambient temperature and relative humidity in the test room were measured approximately 1 m above the top of the fuel cell enclosure and approximately 1 m away from the air inlet side of the micro-cogeneration device.

As detailed in the next section, the bias and precision errors from the primary measurements outlined above (e.g. temperatures, flow rates) propagate through into the derived quantities (e.g. $(UA)_{eff}$ of Eq. (1)). In order to minimize the bias errors, a number of the instruments described above were calibrated. These include the water flow meter, the thermocouples at the heat exchanger's water inlet and outlet, the AC power flow meter, and the natural gas flow meter. These calibrations were effected by comparing instrument readings to reference instruments and then adjusting offset and slope parameters to adjust the translation of voltage signals to measured quantities.

Instantaneous measurements of the FCPM's DC power production, the FCPM's air and fuel supply rates, and the power flow to the battery were taken every second and the averages over the minute were logged to file. All other measurements were taken every 15 s and the four values averaged to log the data at each minute. The condensate flow rate was logged at the same frequency, but using a separate data acquisition system. Each of these measurements records the number of times the bucket had been tilted during the preceding minute. The time stamps in each file were used to synchronize the measurements.

Infrared images of the micro-cogeneration device were captured during one test at which the device was producing its maximum power. Three of the four side faces and the top of the SOFC micro-cogeneration device's enclosure provided unobstructed views for the imaging. These images were used to derive thermal contour maps by taking into account the surface emissivities.

A gas chromatograph was used to analyze the content of the natural gas supply a few days prior to the experiments. This determined the molar fractions of each constituent of the gas supply in order to accurately determine its lower heating value.

4. Calculation of calibration data and analysis of uncertainties

The previous section detailed the measurements taken during the experiments. In order to calibrate the model, these primary

measurements were used to derive the variables of interest to the model. This section details the calculation of these derived quantities and their associated uncertainties. The methods illustrated here for treating the exhaust-gas-to-water heat exchanger equally apply to other aspects of the model, such as the electrical efficiency of the FCPM, the DC–AC conversion efficiency of the power conditioning system, etc.

As discussed in Section 2.2, the equation relating the effective product of the heat transfer coefficient and area to the flow rates of water and gas through the heat exchanger (refer to Eq. (3)) must be calibrated from the experimental data. Referring to Eqs. (1) and (2), it can be shown that $(UA)_{\text{eff}}$ can be derived from five of the primary measurements described in Section 3,

$$(UA)_{\text{eff}} = \frac{(\dot{N}\hat{c}_{\text{P}})_{\text{w-in}}(T_{\text{w-out}} - T_{\text{w-in}})}{\left[\frac{(T_{\text{g-in}}-T_{\text{w-out}})-(T_{\text{g-out}}-T_{\text{w-in}})}{\ln\left(\frac{T_{\text{g-in}}-T_{\text{w-out}}}{T_{\text{g-out}}-T_{\text{w-in}}}\right)}\right]} \tag{13}$$

Eq. (13) was evaluated for each minute of recorded data using the four temperature readings ($T_{\text{w-in}}$, $T_{\text{w-out}}$, $T_{\text{g-in}}$, $T_{\text{g-out}}$) and the water flow rate measurement ($\dot{N}_{\text{w-in}}$). The heat capacity of the water entering the heat exchanger ($\hat{c}_{\text{P,w-in}}$) was calculated from $T_{\text{w-in}}$ using a parametric relation [26].

The method recommended by the American Society of Mechanical Engineers (described in [30] and [31]) was used to calculate the uncertainties of the measured quantities and to propagate these uncertainties into the derived quantities. With this a bias error was assigned to each primary measurement. These were established based upon the instrumentation specifications as either an absolute error as a percent of full-scale measurement and/or a reading error as a percent of the value measured. Where instruments were calibrated (refer to Section 3) the bias error was established based upon the calibration parameters. In these cases, the bias error was set based upon either the average or maximum deviation of the corrected measured values to the reference values.

In some cases additional bias errors were assigned based upon judgement. For example, a substantial bias error was assigned to the velocity measurement of the combined exhaust gas stream due to the restrictions on instrument placement, as discussed in Section 3. As another example, an additional bias error was assigned to the condensate flow rate measurement. As described in Section 3, condensate is measured by a rain gauge tilt bucket after it is pumped from an internal reservoir. The time lag between the pumping and measurement actions introduced some uncertainty to the condensate flow rate measurement. Consequently a bias error of 50 mL (the approximate volume of the internal reservoir) was assigned to the measurement of the condensate flow over the duration of each experiment.

The total bias for each measurement point is calculated from the individual bias errors for that sensor using the root-sum-square method,

$$B = [B_1^2 + B_2^2 + \cdots + B_k^2]^{1/2} \tag{14}$$

For each of the tests examining the performance of the gas-to-water heat exchanger the desired boundary conditions (e.g. $T_{\text{w-in}}$ and $\dot{N}_{\text{w-in}}$) were held as constant as possible for a period of time and data logged each minute. The precision index of a single measurement within a given test is calculated based on the average value of the observed parameter during that test and the number of logged readings,

$$S = \left[\frac{\sum_{i=1}^{N}(X_i - \bar{X})^2}{N-1}\right]^{1/2} \tag{15}$$

where N is the number of logged readings. It is worth noting that the data were logged at 1-min intervals based upon either 1 s or 15 s instantaneous readings (refer to Section 3). The X_i values of Eq. (15) are the 1-min averaged values since the instantaneous data were not logged. It is also worth noting that S has the same value for each data point within a given test.

The precision index of the average value of a parameter for a given test is lower than that for the individual measurements according to,

$$S_{\text{avg}} = \frac{S}{\sqrt{N}} \tag{16}$$

Finally, the bias and precision indices are combined to express the uncertainty in a measured quantity at the 95% confidence level,

$$U_{95\%} = \sqrt{B^2 + (tS)^2} \tag{17}$$

where t is the standard statistical Student's t-value and is a function of the value of N used in evaluating Eq. (15).

The uncertainty of a derived quantity is determined by propagating the bias and precision indices of the measurements that are used to calculate the derived quantity. For example, the bias error for $(UA)_{\text{eff}}$ is calculated as follows (refer to Eq. (13)),

$$B_{(UA)_{\text{eff}}} = \left[\left(\frac{\partial(UA)_{\text{eff}}}{\partial\dot{N}_{\text{w-in}}}B_{\dot{N}_{\text{w-in}}}\right)^2 + \left(\frac{\partial(UA)_{\text{eff}}}{\partial T_{\text{w-out}}}B_{T_{\text{w-out}}}\right)^2 + \left(\frac{\partial(UA)_{\text{eff}}}{\partial T_{\text{w-in}}}B_{T_{\text{w-in}}}\right)^2 + \left(\frac{\partial(UA)_{\text{eff}}}{\partial T_{\text{g-in}}}B_{T_{\text{g-in}}}\right)^2 + \left(\frac{\partial(UA)_{\text{eff}}}{\partial T_{\text{g-out}}}B_{T_{\text{g-out}}}\right)^2\right]^{1/2} \tag{18}$$

The precision index for $(UA)_{\text{eff}}$ is determined in a similar manner and the overall uncertainty determined using Eq. (17).

The propagation of measurement uncertainties into Eq. (18) is demonstrated by examining the test that was illustrated in Fig. 4. The bias errors and precision indices for the four temperature and one water flow rate measurements used in the equation are summarized in Table 1. The bias errors reported in the table are the average for the 82 measurement points of the test. Likewise, the precision index is that corresponding to each individual measurement, and not the precision index of the set average (i.e. it represents S of Eq. (15), not S_{avg} of Eq. (16)).

Table 1 also lists the average uncertainty at the 95% confidence level of the 82 measurements of each of the five parameters. As can be seen, the precision indices are the predominant determinant of the uncertainty of the water temperature measurements, an obser-

Table 1
Uncertainty parameters for test at $T_{\text{w-in}} = 30\,^{\circ}\text{C}$ and $\dot{N}_{\text{w}} = 0.004\,\text{kmol/s}$.

Measurement	Average value over test	B	S	$U_{95\%}$
$T_{\text{w-in}}$	30.60 °C	0.10 °C	0.58 °C	1.17 °C
$T_{\text{w-out}}$	43.38 °C	0.10 °C	0.48 °C	0.97 °C
$T_{\text{g-in}}$	284.27 °C	2.20 °C	0.57 °C	2.48 °C
$T_{\text{g-out}}$	45.04 °C	2.20 °C	0.36 °C	2.32 °C
$\dot{N}_{\text{w}}$ (kmol s)	4.0×10^{-3}	7.9×10^{-5}	2.7×10^{-5}	9.3×10^{-5}

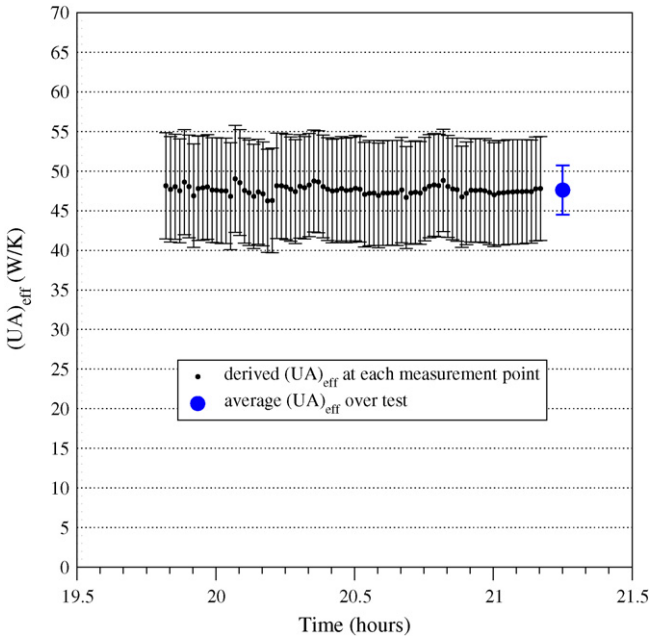

Fig. 5. Derived $(UA)_{eff}$ values and associated 95% error bars for $T_{w-in} = 30\,^{\circ}C$ and $\dot{N}_w = 0.004\,kmol/s$.

vation consistent with the T_{w-in} measurements plotted in Fig. 4. In contrast, the instrument bias errors are the predominant determinants of the uncertainty of the gas temperatures and the water flow rate.

Eq. (13) was applied to calculate the $(UA)_{eff}$ value for each of the 82 measurement points of the test. The procedure outlined in Eqs. (14), (15), (17), and (18) was then applied to calculate the uncertainty for each of these 82 derived $(UA)_{eff}$ values. Fig. 5 plots these derived values and their uncertainties. The test-averaged $(UA)_{eff}$ value determined from the 82 measurement points and its error bar are also shown in the figure. The uncertainty of the test-averaged $(UA)_{eff}$ value is less than that for individual measurements due to Eq. (16).

The procedure outlined in this section was applied to each test to produce sets of test-averaged derived quantities (e.g. $(UA)_{eff}$, ε_{el}, λ) for various combinations of the boundary conditions (e.g. T_{w-in}, $\dot{N}_w$, P_{el}). The calibration of the model using these sets of data is the subject of the next section.

5. Model calibration

This section treats the calibration of the model inputs described in Section 2 using the measured and derived data described in Sections 3 and 4.

5.1. Exhaust-gas-to-water heat exchanger

The experiments yielded 17 derived values of $(UA)_{eff}$ at various water ($\dot{N}_w$) and gas ($\dot{N}_g$) flow rates. A non-linear regression method was used to establish the values of the $hx_{s,i}$ coefficients that produced the best fit of these data to Eq. (3). The values of the coefficients determined from this analysis are presented in Table 2.

It is important to note that the test-averaged derived $(UA)_{eff}$, $\dot{N}_w$, and $\dot{N}_g$ values (refer to Section 4) were used to regress these coefficients. As a non-linear regression method was used it is not possible to propagate uncertainties in these values into the $hx_{s,i}$ coefficients using the methods elaborated in Section 4. However, despite the deterministic appearance of the coefficients in Table 2, the regressions inherently contain uncertainty and this level of uncertainty is commensurate with the uncertainty of the derived $(UA)_{eff}$, $\dot{N}_w$, and $\dot{N}_g$ values.

Fig. 6 compares the $(UA)_{eff}$ determined with Eq. (3) and the coefficients of Table 2 with the $(UA)_{eff}$ values derived from the measurements. The uncertainty bars determined in Section 4 are plotted in the figure. The left side of the figure provides a view normal to the $\dot{N}_g$ axis while the right side provides a view normal to the $\dot{N}_w$ axis. As can be seen, the functional form of Eq. (3) well represents the dependency of $(UA)_{eff}$ on the two flow rates. The calibrated values lie within the error bars for each of the 17 data points.

Fig. 7 provides another indication of the goodness of fit between the calibrated $(UA)_{eff}$ values and those derived from measurements. The coefficient of determination (r^2 value) was 0.98. The average error (difference between the calibrated $(UA)_{eff}$ value and that derived from measurements) was 1.9% while the root-mean-square error was 2.1%. The maximum error for a single point was 3.2%.

A number of tests, in addition to the 17 described above, were conducted to explore the operation of the heat exchanger under condensing conditions. One of these tests was configured to identify $T_{cond-threshold}$ of Eq. (5). This variable represents the threshold of the water inlet temperature above which condensation does not occur. The examination of the tilt bucket readings during preliminary testing indicated an approximate range within which $T_{cond-threshold}$ lay. However, each of these tests was time consuming. As elaborated in Section 3, the tilt bucket instrument was filled only after the cogeneration device's internal condensate reservoir became filled and was pumped out. Steady conditions had to be held for long periods of time (in some cases many hours) in order to register readings at the tilt bucket.

Section 3 explained how the formation of condensation from the exhaust gases led to erroneous T_{g-in} thermocouple readings. Advantage was taken of this fact to calibrate $T_{cond-threshold}$ for Eq. (5). By controlling the water loop illustrated in Fig. 3, T_{w-in} was slowly reduced from 33 °C, which the preliminary testing had indicated was above $T_{cond-threshold}$. For the FCPM's electrical output exercised in this test, T_{g-in} was approximately 280 °C. As shown in Fig. 8 the thermocouple produced reliable data for the first portion

Table 2
Calibrated coefficients.

Gas-to-water heat exchanger sensible coefficients for Eq. (3)	$hx_{s,0} = 83.1$; $hx_{s,1} = 4\,798$; $hx_{s,2} = -138 \times 10^3$; $hx_{s,3} = -353.8 \times 10^3$; $hx_{s,4} = -5.15 \times 10^8$
Gas-to-water heat exchanger latent coefficients for Eq. (5)	$hx_{l,1} = -1.96 \times 10^{-4}$; $hx_{l,2} = 3.1 \times 10^{-3}$; $T_{cond-threshold} = 35\,^{\circ}C$
FCPM electrical efficiency coefficients for Eq. (9)	$\varepsilon_0 = 0.642388$; $\varepsilon_1 = -1.619 \times 10^{-4}$; $\varepsilon_2 = 2.26007 \times 10^{-8}$
FCPM air supply coefficients for Eq. (12)	$a_0 = 1.50976 \times 10^{-3}$; $a_1 = -7.76656 \times 10^{-7}$; $a_2 = 1.30317 \times 10^{-10}$; $a_3 = 2.83507 \times 10^{-3}$
Range of applicability:	
$5.2\,^{\circ}C \le T_{water,in} \le 59.8\,^{\circ}C$	
$3.63 \times 10^{-3}\,kmol/s \le \dot{N}_{water} \le 1.09 \times 10^{-2}\,kmol/s$	
$3010\,W \le P_{el} \le 3728\,W$	
$10.0\,^{\circ}C \le T_{air} \le 24.2\,^{\circ}C$	
$T_{room} \approx 22\,^{\circ}C$	

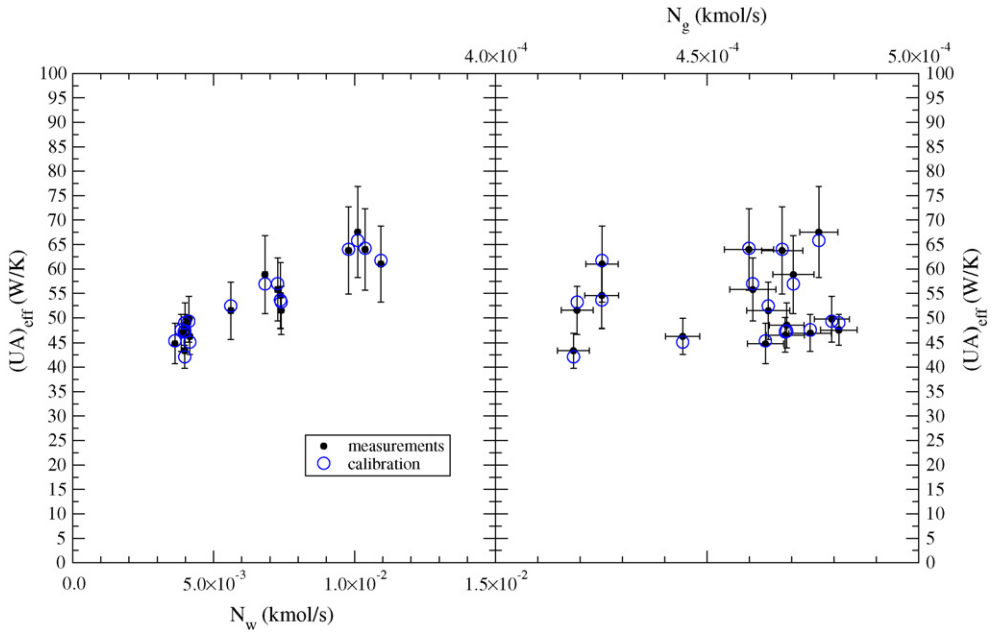

Fig. 6. Calibrated $(UA)_{eff}$ versus measurements as a function of $\dot{N}_w$ (left) and $\dot{N}_g$ (right).

of the test. (It should have read approximately 280 °C throughout the test.) The thermocouple, however, began producing unreliable readings once T_{w-in} was reduced to 23 °C. This event indicated the first formation of liquid water which dripped onto the thermocouple. Even as the inlet water temperature was warmed to 35 °C, the thermocouple continued to produce unreliable readings, indicating that condensation continued to occur. It took considerable time for the thermocouple readings to stabilize. This tends to indicate that although the onset of condensation requires a low value of T_{w-in}, once condensing conditions have been achieved condensation can occur at warmer temperatures. Based upon this test it was decided to set $T_{cond-threshold}$ to 35 °C.

A series of seven tests were then conducted at various water flow rates and values of T_{w-in} in order to establish the $hx_{l,i}$ coefficients of Eq. (5). Sufficient time was allowed in each test to achieve steady conditions. Due to practical constraints, however, these tests could only be conducted with a nearly constant ratio of water vapour in the exhaust gas stream (refer to $\dot{N}_{H_2O}/\dot{N}_{g-in}$ in Eq. (5)). (This is determined by the FCPM's operating point.)

A non-linear regression method was used to establish the values of the $hx_{l,i}$ coefficients that produced the best fit to Eq. (5). As elaborated above, $T_{cond-threshold}$ was set to 35 °C to perform this regression. The values of the coefficients determined from this analysis are presented in Table 2.

Fig. 9 compares the $\dot{N}_{H_2O\text{-cond}}$ determined with Eq. (5) and the coefficients of Table 2 with the $\dot{N}_{H_2O\text{-cond}}$ values derived from

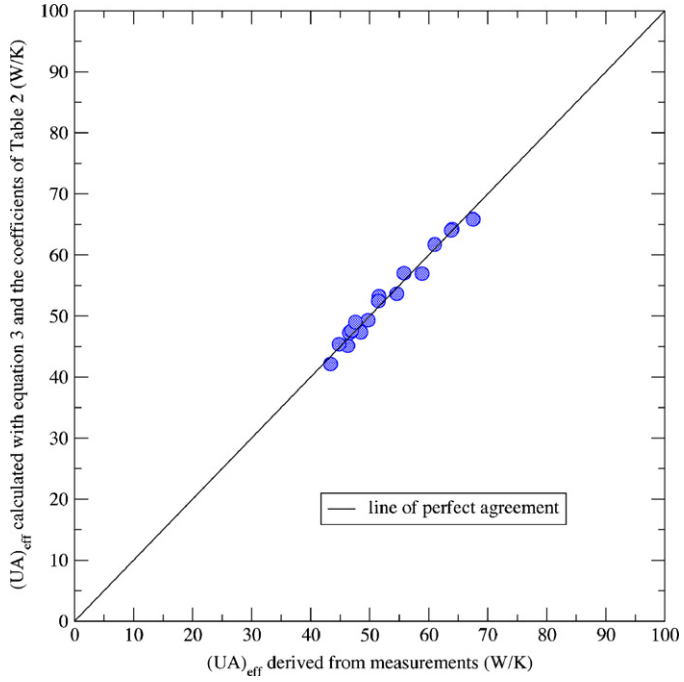

Fig. 7. Goodness of fit between calibrated and measured $(UA)_{eff}$.

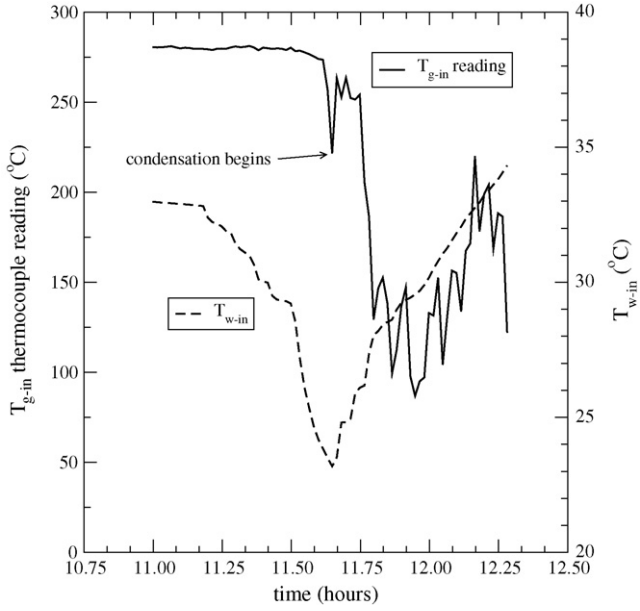

Fig. 8. Identification of $T_{cond-threshold}$.

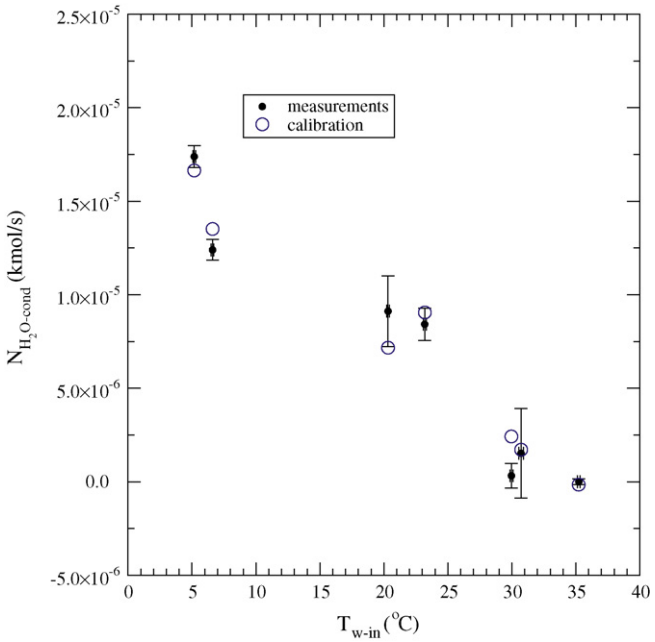

Fig. 9. Goodness of fit between calibrated and measured $\dot{N}_{H_2O-cond}$.

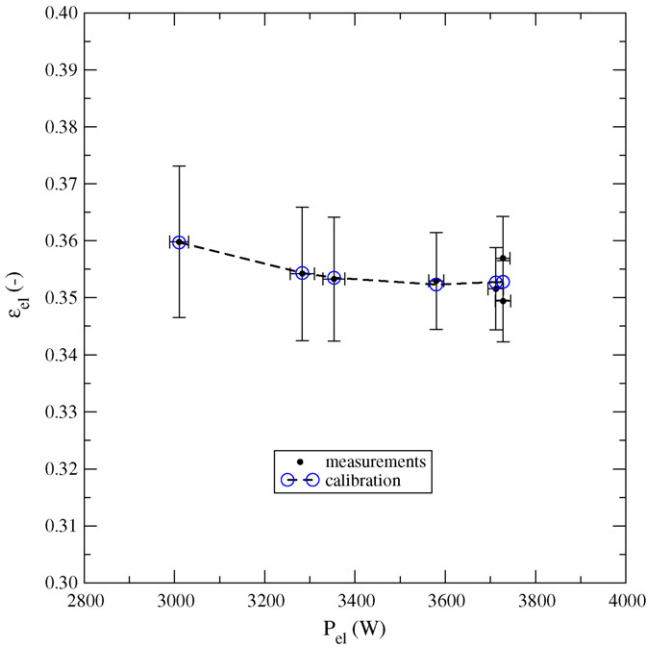

Fig. 10. Calibrated ε_{el} versus measurements.

the measurements. The coefficient of determination (r^2 value) was 0.96. The average error (difference between calibrated values and those derived from measurements) was 10^{-6} kmol s^{-1} [5] while the root-mean-square error was 1.2×10^{-6} kmol s^{-1}. The maximum error for a single point was 2.1×10^{-6} kmol s^{-1}. The uncertainty bars determined in Section 4 are plotted in the figure. As can be seen, the functional form of Eq. (5) reasonably represents the dependency of $\dot{N}_{H_2O\text{-cond}}$ upon T_{w-in}. The calibrated values lie within the error bars for five of the seven data points. The greatest deviation between measurement and calibration occurs at $T_{w-in} \approx 30\,^{\circ}C$ where the condensation flow rate is very small.

5.2. Fuel cell power module electrical efficiency

Data from seven experiments were used to calibrate the FCPM electrical efficiency to the net DC power production (refer to Eq. (9)). A non-linear regression method was used to establish the values of the ε_i coefficients that produced the best fit to Eq. (9). The values of the coefficients determined from this analysis are presented in Table 2. This table also presents the range of P_{el} for which the correlation is applicable.

Fig. 10 compares the ε_{el} determined with Eq. (8) and the coefficients of Table 2 with the ε_{el} values derived from the measurements. The $U_{95\%}$ uncertainty bars are plotted in the figure. The coefficient of determination (r^2 value) was 0.58. The average error (difference between the calibrated ε_{el} value and that derived from measurements) was 0.4% (in relative terms) while the root-mean-square error was 0.6%. The maximum error for a single point was 1.2%.

5.3. Fuel cell power module air supply

Data from 28 experiments were used to calibrate the excess air ratio of the FCPM air supply. A non-linear regression method was used to establish the values of the a_i coefficients that produced the best fit to Eq. (12). The values of the coefficients determined from this analysis are presented in Table 2. This table also presents the range of P_{el} and T_{air} for which the correlation is applicable.

Fig. 11 compares the $\dot{N}_{air}$ determined with Eq. (12) and the coefficients of Table 2 with the $\dot{N}_{air}$ values derived from the measurements. The $U_{95\%}$ uncertainty bars are plotted in the figure. The coefficient of determination (r^2 value) was 0.77. The average error (difference between the calibrated $\dot{N}_{air}$ value and that derived from measurements) was 2.3% while the root-mean-square error was 2.8%. The maximum error for a single point was 5.6%. As Fig. 11 illustrates, for some of the 28 points the deviation between

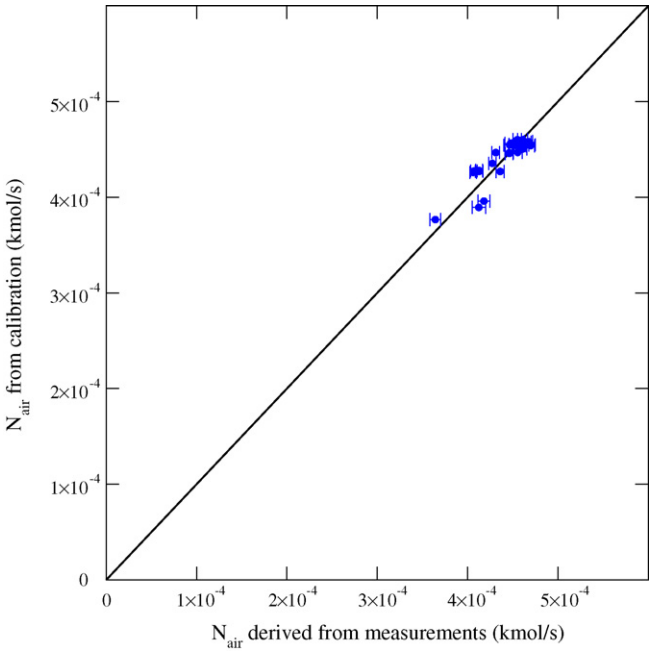

Fig. 11. Calibrated $\dot{N}_{air}$ versus measurements.

[5] To place these numbers in context, a condensation rate of 10^{-6} kmol/s results in approximately 40 W of heat transfer.

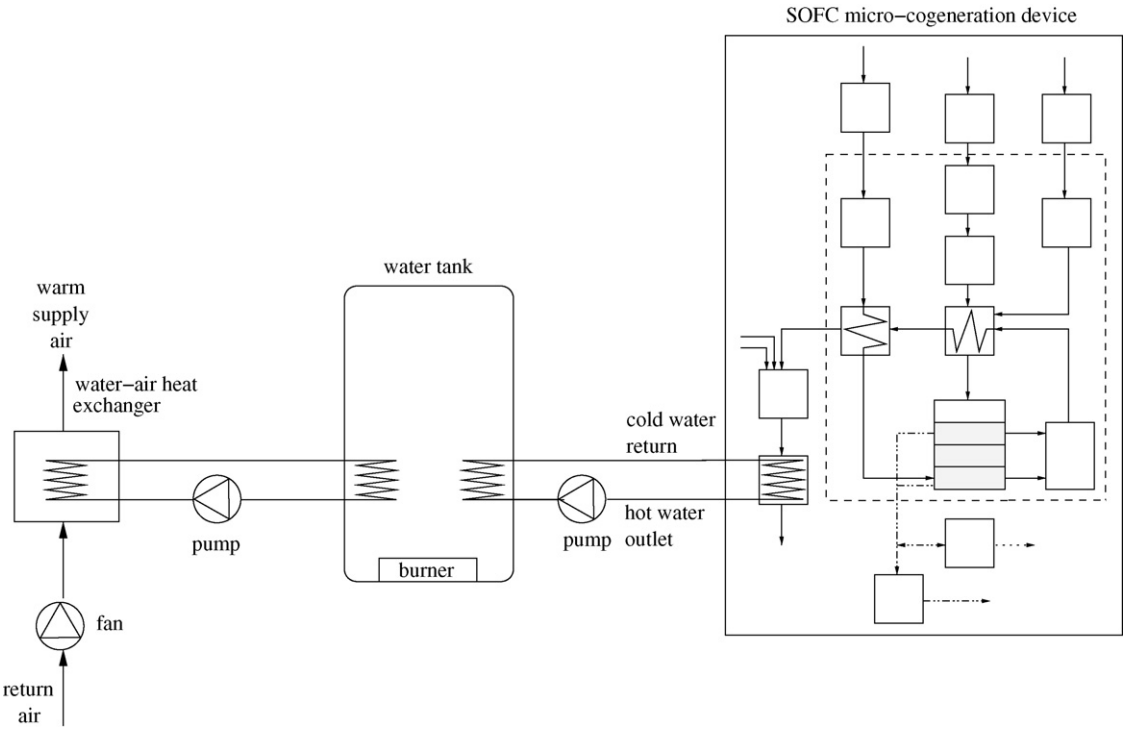

Fig. 12. Configuration of a SOFC micro-cogeneration heating plant.

the calibration and the experimentally derived values exceeds the measurement uncertainty. This result indicates the potential for improvements to the form of Eq. (12), although additional data under a greater range of operating conditions would be required to explore this.

6. Demonstrated application of calibrated model

The process elaborated in the previous section was repeated for all aspects of the model. The interested reader is referred to [29] which provides the complete set of calibration parameters to accurately represent the performance of this 2.8 kW_{AC} SOFC micro-cogeneration device.

The calibrated model can now be used to accurately simulate the thermal and electrical performance of this prototype device when coupled to a house's thermal plant. This is demonstrated through the use of the ESP-r simulation program [9], which includes the IEA/ECBCS Annex 42 model, in conjunction with the calibration parameters presented in this paper. An ESP-r simulation model was configured to represent a typical 20–30- year-old detached two-storey Canadian house with 160 m^2 of conditioned floor area. When conditioned to 21 °C and simulated with Ottawa weather data, the house has an annual space heating demand of 78 GJ, which is typical of this vintage of construction, house size, and location.

The SOFC micro-cogeneration device is coupled to supporting plant components as illustrated in Fig. 12 in order to provide the house's space heating. The thermal output of the SOFC micro-cogeneration device is transferred to a water storage tank by a circulating pump. When the house's temperature drops below 20.5 °C, the second pump cycles on to circulate hot water from the tank through a water-to-air heat exchanger. Likewise, the fan cycles on to circulate air from the house through the heat exchanger and delivers this warmed air to heat the house.

The tank's make-up burner cycles on when then tank temperature drops below 50 °C. To avoid excessive temperatures, energy is extracted from the tank and rejected to the environment when its temperature rises to 92 °C. The SOFC micro-cogeneration device is assumed to operate continuously throughout the year producing 2.8 kW of AC power. It is assumed that the house can export power to the central electrical grid when there is a surplus of power, and import from the grid when there is a deficit.

An annual simulation conducted with this configuration using Ottawa weather data predicted that 9366 m^3 of natural gas would be consumed by the SOFC while another 745 m^3 would be consumed by the make-up burner. Over the year, the SOFC micro-cogeneration device would generate more than two and a half times the electrical demands of the occupants and plant equipment (pumps and fan), resulting in a net export of 53.4 GJ of electricity to the central grid. Due to temporal mismatches between electrical production and demand, some importation from the grid would also be required. The monthly integrated electrical balance is illustrated in Fig. 13.

Some important observations regarding the suitability of this configuration can be drawn by examining the monthly integrated thermal energy balance on the water tank (see Fig. 14). As can be seen, during the winter months the SOFC micro-cogeneration device's thermal output is insufficient to meet the house's space heating demand. Consequently, extensive use of the tank's make-up burner is required. During this period, the tank never overheats and thus no dumping of heat is required. During the summer, however, the vast majority of the SOFC micro-cogeneration device's thermal output is wasted. There is also significant dumping of heat during the spring and autumn due to temporal mismatches between thermal production by the SOFC micro-cogeneration device and space heating demands. During this period, the make-up burner often cycles on in the early morning to meet space heating demands, while the heat dumping facility is activated later in the day. Fully 36.5% of the SOFC micro-cogeneration device's thermal output is wasted through the heat dump facility while another 9% is lost due to heat transfer from the tank's external surfaces to the containing room.

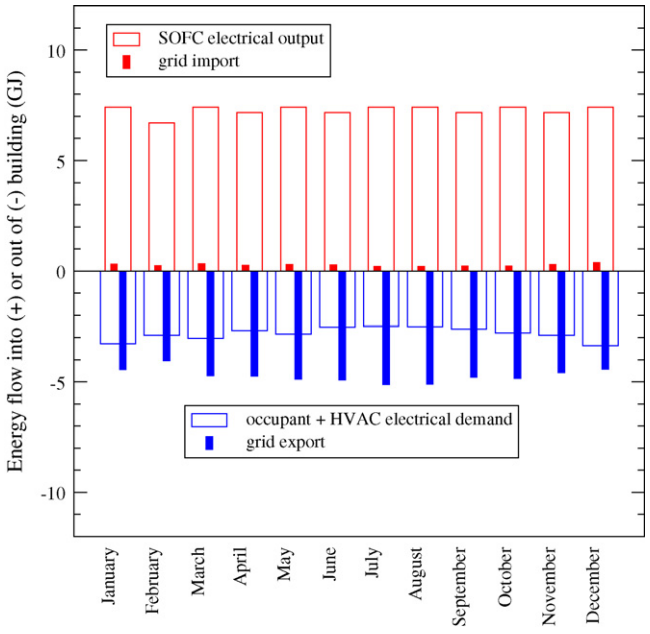

Fig. 13. Monthly integrated electrical balance for house with SOFC micro-cogeneration device.

These simulation results identify a number of areas where the performance of the SOFC micro-cogeneration-based heating system might be improved to increase overall system efficiency. Further analysis with the calibrated model could lead to improvements in the design and operation of the coupling between the SOFC micro-cogeneration device and the heating plant. Alternate schemes for utilizing the SOFC micro-cogeneration device's thermal output, such as DHW heating and/or thermally activated cooling, could be explored. The potential impact of design improvements to sub-systems, such as the DC–AC power conditioner or gas-to-water heat exchanger, could be explored by adjusting some of the calibration coefficients determined in Section 5. Hypothetical

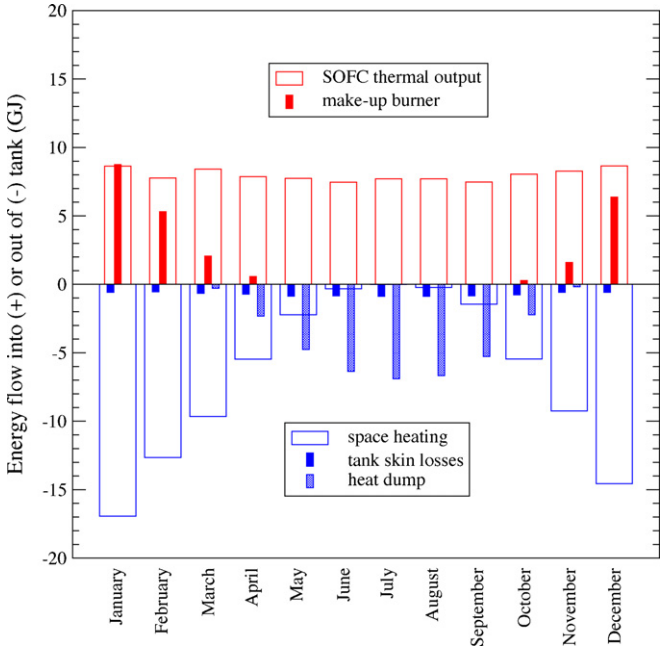

Fig. 14. Monthly integrated thermal energy balance on tank coupled to SOFC micro-cogeneration device.

devices could be analyzed if methods existed to establish appropriate coefficients for the model's sub-systems. This would enable analyses focused upon optimizing the output capacity and control of SOFC micro-cogeneration devices at early stages of design.

7. Conclusions

Previous research has produced a mathematical model for simulating the thermal and electrical performance of SOFC micro-cogeneration devices and which is suitable for use in whole-building simulation programs. This is a system-level model that considers the thermodynamic performance of all components that consume energy and produce the SOFC micro-cogeneration device's thermal and electrical output. Each of the model's nine control volumes represents a sub-system that produces electrical power, supplies air, captures heat from the hot product gases, etc.

Through example, this paper has demonstrated how this model can be calibrated to represent the performance of specific SOFC micro-cogeneration devices. The experimental procedures that were employed to test a prototype 2.8 kW_{AC} SOFC micro-cogeneration system were described in detail. The experimental configuration, types of instrumentation employed, and the operating scenarios examined were treated. The propagation of measurement uncertainty into the derived quantities that are necessary for model calibration was demonstrated by focusing upon the SOFC micro-cogeneration system's gas-to-water heat exchanger. The calibration of the model's empirical coefficients was then demonstrated. The results of this calibration approach were presented for the gas-to-water heat exchanger, and for the fuel cell power module's electrical conversion efficiency and air supply. Although not presented here, the same methods and experimental data were used to calibrate the other aspects of the model for this prototype device, namely its transient response, its DC–AC power conditioning system, its dilution air system, and its thermal losses. The reader is cautioned that the calibrated empirical coefficients presented in this paper are only valid within the ranges of independent variables examined in the experiments.

The result of this work is a calibrated model that can accurately simulate the thermal and electrical performance of this 2.8 kW_{AC} SOFC micro-cogeneration device when coupled to a house's thermal plant. An illustration of the types of analyses that have been enabled with this work was given by focusing upon the integration of a SOFC micro-cogeneration device with a house's space heating system. This demonstration of the modelling capabilities revealed a number of areas where the performance of the SOFC micro-cogeneration-based heating system might be improved to increase overall system efficiency and described how the model could inform the design and development process for SOFC micro-cogeneration devices.

A total of 45 experiments were conducted to gather the necessary data to calibrate the model for the 2.8 kW_{AC} SOFC micro-cogeneration device. The results presented here have demonstrated that the mathematical form of the individual terms of the model well represents the functional dependency upon the independent variables. However, these results do not speak to the validity of the calibrated model to accurately predict performance under operating regimes other than those examined during the 45 experiments. In fact 16 additional experiments were conducted (disjunct from the 45 experiments used to calibrate the model) to empirically validate the model and its calibration, the results of which will be reported in a future paper.

Future research will apply the calibrated model to examine the thermal and electrical performance of the 2.8 kW_{AC} SOFC micro-cogeneration device in various residential buildings, in various climates, and under various operating scenarios to contrast the per-

formance of the technology to conventional heating and electrical supply systems. Using the techniques described here, the model will also be calibrated to represent the performance of other prototype SOFC micro-cogeneration devices and configured to represent hypothetical devices to guide research and development efforts.

Acknowledgements

The work described in this paper was undertaken as part of IEA/ECBCS Annex 42 (http://www.cogen-sim.net). The Annex was an international collaborative research effort and the authors gratefully acknowledge the indirect or direct contributions of the other Annex participants.

References

[1] I. Knight, V. Ugursal (Eds.), Residential Cogeneration Systems: A Review of the Current Technologies, IEA/ECBCS Annex 42 Report, 2005, ISBN No. 0-662-40482-3.
[2] H. Onovwiona, V. Ugursal, Residential cogeneration systems: review of the current technology, Renewable and Sustainable Energy Reviews 10 (5) (2006) 389–431.
[3] E. Entchev, J. Gusdorf, M. Swinton, M. Bell, F. Szadkowski, W. Kalbfleisch, R. Marchand, Micro-generation technology assessment for housing technology, Energy and Buildings 36 (9) (2004) 925–931.
[4] Anonymous, Micro-chp accelerator: Interim report, Tech. rep., Carbon Trust, UK, CTC726 (November 2007).
[5] I. Beausoleil-Morrison (Ed.), An Experimental and Simulation-Based Investigation of the Performance of Small-Scale Fuel Cell and Combustion-Based Cogeneration Devices Serving Residential Buildings, IEA/ECBCS Annex 42 Report, 2008, ISBN No. 978-0-662-47923-9.
[6] R. Braun, S. Klein, D. Reindl, Evaluation of system configurations for solid oxide fuel cell-based micro-combined heat and power generators in residential applications, Journal of Power Sources 158 (2) (2006) 1290–1305.
[7] U.C. Colpier, D. Cornland, The economics of the combined cycle gas turbine–an experience curve analysis, Energy Policy 30 (4) (2002) 309–316.
[8] T. DeMoss, They're he-e-re (almost): the 60% efficient combined cycle, Power Engineering 100 (7) (1996) 17–21.
[9] J. Clarke, Energy Simulation in Building Design, 2nd ed., Butterworth-Heinemann, Oxford, UK, 2001.
[10] D. Crawley, L. Lawrie, F. Winkelmann, W. Buhl, Y. Huang, C. Pedersen, R. Strand, R. Liesen, D. Fisher, M. Witte, J. Glazer, Energyplus: creating a new-generation building energy simulation program, Energy and Buildings 33 (2001) 319–331.
[11] Solar Energy Laboratory, TRNSYS 16, a transient system simulation program, Tech. rep., University of Wisconsin, Madison USA (2004).
[12] V. Dorer, R. Weber, A. Weber, Performance assessment of fuel cell micro-cogeneration systems for residential buildings, Energy and Buildings 37 (2005) 1132–1146.
[13] A. Hawkes, M. Leach, Solid oxide fuel cell systems for residential micro-combined heat and power in the UK: key economic drivers, Journal of Power Sources 149 (2005) 72–83.
[14] B. Sicre, A. Bühring, B. Platzer, Energy and financial performance of micro-chp in connection with high-performance buildings, in: Proceedings of Building Simulation 2005, Montréal, Canada, 2005, pp. 1131–1138.
[15] K. Alanne, A. Saari, V. Ugursal, J. Good, The financial viability of an SOFC cogeneration system in single-family dwellings, Journal of Power Sources 158 (2006) 403–416.
[16] J. Cockroft, N. Kelly, A comparative assessment of future heat and power sources for the UK domestic sector, Energy Conversion and Management 47 (2006) 2349–2360.
[17] A. Peacock, M. Newborough, Impact of micro-combined heat-and-power systems on energy flows in the UK electricity supply industry, Energy 31 (2006) 1804–1818.
[18] P. Boait, R. Rylatt, M. Stokes, Optimisation of consumer benefits from micro combined heat and power, Energy and Buildings 38 (2006) 981–987.
[19] R. Possidente, C. Roselli, M. Sasso, S. Sibilio, Experimental analysis of micro cogeneration units based on reciprocating internal combustion engine, Energy and Buildings 38 (2006) 1417–1422.
[20] A. Hawkes, M. Leach, Cost-effective operating strategy for residential micro combined heat and power, Energy 32 (2007) 711–723.
[21] S. Sibilio, M. Sasso, R. Possidente, C. Roselli, Assessment of micro-cogeneration potential for domestic trigeneration, International Journal of Environmental Technology and Management 7 (1–2) (2007) 147–164.
[22] A. Hawkes, P. Aguiar, B. Croxford, M. Leach, C. Adjiman, N. Brandon, Solid oxide fuel cell micro combined heat and power system operating strategy: Options for provision of residential space and water heating, Journal of Power Sources 164 (2007) 260–271.
[23] M. De Paepe, D. Mertens, Combined heat and power in a liberalised energy market, Energy Conversion and Management 48 (2007) 2542–2555.
[24] E.M.B. Maalla, P.L. Kunsch, Simulation of micro-chp diffusion by means of system dynamics, Energy Policy 36 (7) (2008) 2308–2319.
[25] I. Beausoleil-Morrison, A. Schatz, F. Maréchal, A model for simulating the thermal and electrical production of small-scale solid-oxide fuel cell cogeneration systems within building simulation programs, J HVAC&R Research Special Issue 12 (3a) (2006) 641–667.
[26] N. Kelly, I. Beausoleil-Morrison (Eds.), Specifications for Modelling Fuel Cell and Combustion-Based Residential Cogeneration Devices within Whole-Building Simulation Programs, IEA/ECBCS Annex 42 Report, 2007, ISBN No. 978-0-662-47116-5.
[27] S. Beale, Y. Lin, S. Zhubrin, W. Dong, Computer methods for performance prediction in fuel cells, Journal of Power Sources 118 (2003) 79–85.
[28] R. Bove, P. Lunghi, N. Sammes, SOFC mathematical model for systems simulations. Part 1. From a micro-detailed to macro-black-box model, International Journal of Hydrogen Energy 30 (2005) 181–187.
[29] I. Beausoleil-Morrison (Ed.), Experimental Investigations of Residential Cogeneration Devices and Model Calibration, IEA/ECBCS Annex 42 Report, 2007, ISBN No. 978-0-662-47523-1.
[30] R. Abernethy, R. Benedict, R. Dowdell, ASME measurement uncertainty, Journal of Fluids Engineering 107 (1985) 161–164.
[31] R. Moffat, Describing the uncertainties in experimental results, Experimental Thermal and Fluid Science 1 (1988) 3–17.